

Few-Layer $\text{Fe}_3(\text{PO}_4)_2 \cdot 8\text{H}_2\text{O}$: Novel H-Bonded 2D Material and Its Abnormal Electronic Properties

Sibai Li,[†] Ruge Quhe,^{‡,§} Mouyi Weng,[†] Yancong Feng,[†] Yunxing Zuo,[†] Weiji Xiao,[†] Jiaxin Zheng,^{*,†} Jing Lu,[‡] and Feng Pan^{*,†}

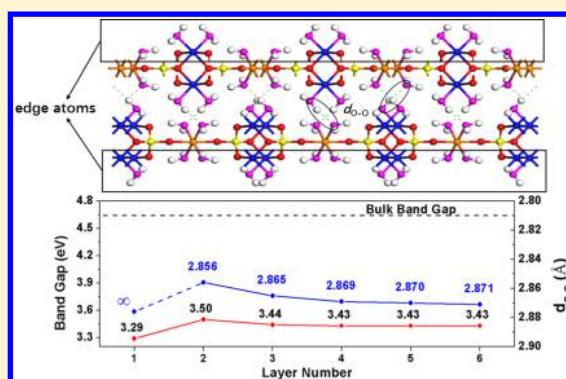
[†]School of Advanced Materials, Peking University Shenzhen Graduate School, Shenzhen518055, China

[‡]State Key Laboratory of Mesoscopic Physics and Department of Physics, Peking University, Beijing100871, P. R. China

[§]State Key Laboratory of Information Photonics and Optical Communications, Beijing University of Posts and Telecommunications & School of Science, Beijing100876, China

Supporting Information

ABSTRACT: Using first-principles calculations, we study the structural and electronic properties of a new layered hydrogen-bonded 2D material $\text{Fe}_3(\text{PO}_4)_2 \cdot 8\text{H}_2\text{O}$. Interestingly, unlike other common 2D materials, such as layered van der Waals 2D materials, the band gap of 2D $\text{Fe}_3(\text{PO}_4)_2 \cdot 8\text{H}_2\text{O}$ -(010)-(1 × 1) is smaller than bulk $\text{Fe}_3(\text{PO}_4)_2 \cdot 8\text{H}_2\text{O}$, which does not obey the normal quantum confinement effect and can be attributed to the edge states and the hydrogen bonds between the layers. We also find that the band-gap variation with the reduced layers depends on the length of the interlayer hydrogen bond and the stronger interlayer hydrogen bond leads to the larger band gap.



I. INTRODUCTION

Since the discovery of graphene,¹ 2D materials that are a few layers thick have been intensively studied for, different from bulk materials, their various applications and attractive properties. A variety of prototype devices with excellent performances based on 2D materials have been fabricated, such as field-effect transistors (FETs),^{2–4} sensors,⁵ lithium-ion batteries,⁶ supercapacitors,⁷ valleytronic devices,⁸ and so on. These 2D materials can be divided into two classes: layered van der Waals solids, such as graphene¹ and transition-metal dichalcogenides (TMDs),^{9,10} and layered ionic solids, such as $\text{KLn}_2\text{Ti}_3\text{O}_{10}$,¹¹ LiCoO_2 ,¹² and $\text{Eu}(\text{OH})_{2.5}\text{Cl}_{0.5}$.¹³ Because of the quantum confinement effect, the band gap of most 2D materials, such as TMDs, is larger than bulk materials as the layer number decreases.¹⁴

Recently, we successfully synthesized 2D $\text{Fe}_3(\text{PO}_4)_2 \cdot 8\text{H}_2\text{O}$ sheets by means of a simple chemically induced precipitation method and postprocessing for the first time and found its application as an excellent cathode material for lithium-ion batteries¹⁵ and sodium-ion batteries.¹⁶ The bulk vivianite $\text{Fe}_3(\text{PO}_4)_2 \cdot 8\text{H}_2\text{O}$, which has been well studied both experimentally^{17–24} and theoretically,^{25,26} has a monoclinic lattice with $I2/m$ symmetry and with cell parameters $a = 10.021 \text{ \AA}$, $b = 13.441 \text{ \AA}$, $c = 4.721 \text{ \AA}$, and $\beta = 102.84^\circ$.²⁴ The bulk vivianite $\text{Fe}_3(\text{PO}_4)_2 \cdot 8\text{H}_2\text{O}$ is an antiferromagnet with a Neel temperature $T_N \approx 10 \text{ K}$, and above the Neel temperature, it is a paramagnet.¹⁹ Both bulk and 2D $\text{Fe}_3(\text{PO}_4)_2 \cdot 8\text{H}_2\text{O}$ are easily oxidized from Fe^{2+} to Fe^{3+} in the air.^{15,27,28} Different from van der Waals solids, the adjacent sheets consisting of linked Fe and PO_4 polyhedra in bulk

$\text{Fe}_3(\text{PO}_4)_2 \cdot 8\text{H}_2\text{O}$ are combined through hydrogen bonds formed between the H_2O ligands,²³ which may lead to some interesting properties in 2D $\text{Fe}_3(\text{PO}_4)_2 \cdot 8\text{H}_2\text{O}$. Using first-principles calculations, Pinto et al. studied the stability of different $\text{Fe}_3(\text{PO}_4)_2 \cdot 8\text{H}_2\text{O}$ surfaces and their scanning tunneling microscopy (STM) images,²⁵ and the (010) surface was predicted to be the most stable. However, they did not study the electronic properties of 2D $\text{Fe}_3(\text{PO}_4)_2 \cdot 8\text{H}_2\text{O}$. Herein, using first-principles calculations, we investigate the structural and electronic properties of 2D $\text{Fe}_3(\text{PO}_4)_2 \cdot 8\text{H}_2\text{O}$ -(010)-(1 × 1). The electronic properties of one- to six-layer $\text{Fe}_3(\text{PO}_4)_2 \cdot 8\text{H}_2\text{O}$ -(010)-(1 × 1) are calculated, and we find an unexpected outcome about the band gap of 2D $\text{Fe}_3(\text{PO}_4)_2 \cdot 8\text{H}_2\text{O}$ -(010)-(1 × 1), which is different from the common 2D materials.

II. METHODOLOGY

DFT has been performed using plane-wave basis set and projector-augmented wave (PAW) method^{29,30} implemented in the Vienna ab initio simulation package (VASP) code^{31,32} to optimize the structures. The generalized gradient approximation (GGA) functional³³ to the exchange-correction functional of Perdew–Burke–Ernzerhof (PBE).³³ It is well known that HSE06 functional is capable of correctly predicting the band gap and other electronic structures. The band gap of monolayer,

Received: July 26, 2016

Revised: October 2, 2016

Published: November 4, 2016

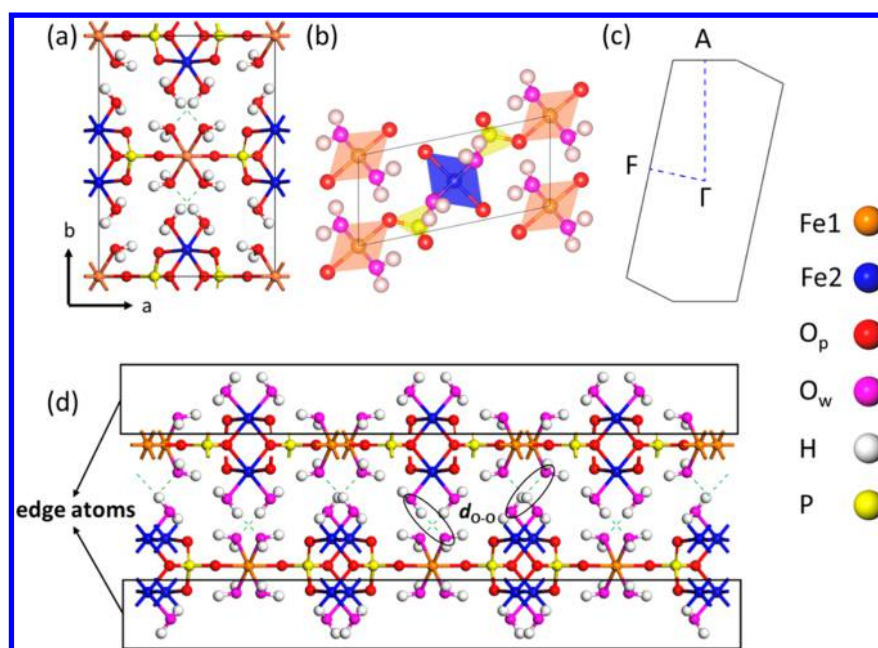


Figure 1. PBE + U (6 eV) optimized structure for paramagnetic $\text{Fe}_3(\text{PO}_4)_2 \cdot 8\text{H}_2\text{O}$. (a) Side views of the bulk $\text{Fe}_3(\text{PO}_4)_2 \cdot 8\text{H}_2\text{O}$. The orange units represent $\text{Fe}_1\text{-O}$ octahedral, the blue units represent $\text{Fe}_2\text{-O}$ octahedra, and the yellow units represent P-O tetrahedral. (b) Top view of the 1L $\text{Fe}_3(\text{PO}_4)_2 \cdot 8\text{H}_2\text{O}$. (c) Brillouin zone of 2D $\text{Fe}_3(\text{PO}_4)_2 \cdot 8\text{H}_2\text{O}$. (d) Side view of the 2L $\text{Fe}_3(\text{PO}_4)_2 \cdot 8\text{H}_2\text{O}$. The green dashed lines denote the interlayer hydrogen bond. The black rectangle denotes the edge atoms. The black ellipse denotes the $d_{\text{O-O}}$.

bilayer, and bulk $\text{Fe}_3(\text{PO}_4)_2 \cdot 8\text{H}_2\text{O}$ predicted by HSE06 is 3.06, 3.32, and 4.55 eV, respectively. Because of the restrictions of using HSE06 on larger system, the PBE + U within Liechtenstein's approach³⁴ is employed to consider the strong on-site Coulomb repulsion. We set the $U = 6.0$ eV because it can reproduce the band gap suggested by HSE06. The plane-wave cut off energy is set to 650 eV to ensure the accuracy. To prevent spurious interaction between periodic images, a vacuum buffer space of at least 20 Å is set. The Brillouin zone is sampled by $4 \times 1 \times 7$ special k-points for slab and $3 \times 3 \times 5$ for bulk, using the Monkhorst Pack scheme³⁵ for optimization, and $8 \times 1 \times 20$ to get the densities of states (DOS). The calculation will not finish until the energy between two successive steps is $<10^{-4}$ eV and the force is <0.025 eV/Å on each atom. We consider different magnetic structures (ferromagnetic, ferrimagnetism, and anti-ferromagnetic) of the monolayer, bilayer, and trilayer $\text{Fe}_3(\text{PO}_4)_2 \cdot 8\text{H}_2\text{O}$ (Table SI, Supporting Information). According to the tiny energy differences between these magnetic structures (\sim meV/atom), we assume 2D $\text{Fe}_3(\text{PO}_4)_2 \cdot 8\text{H}_2\text{O}$ is paramagnetic as bulk $\text{Fe}_3(\text{PO}_4)_2 \cdot 8\text{H}_2\text{O}$.¹⁹ We choose a nonmagnetic (NM) (i.e., non-spin-polarized) to approximate the finite temperature phase of paramagnetic $\text{Fe}_3(\text{PO}_4)_2 \cdot 8\text{H}_2\text{O}$ according to the Stoner theory of magnetism.³⁶

III. RESULTS AND DISCUSSION

A. Geometric Structure of 2D $\text{Fe}_3(\text{PO}_4)_2 \cdot 8\text{H}_2\text{O}$ - (010)-(1 \times 1). Bulk, monolayer (1L), bilayer (2L), trilayer (3L), quadrilayer (4L), pentalayer (5L), and hexalayer (6L) $\text{Fe}_3(\text{PO}_4)_2 \cdot 8\text{H}_2\text{O}$ - (010)-(1 \times 1) are considered. The crystal structures of the bulk and 2D $\text{Fe}_3(\text{PO}_4)_2 \cdot 8\text{H}_2\text{O}$ are shown in Figure 1. We can see two different types of O atoms: O marked by red is coordinated by P and Fe, and O_w marked by pink is coordinated by H and Fe. The interlayer hydrogen bond is formed between adjacent O_w atoms. Also there are two different types of Fe atoms: Fe1 marked by blue is coordinated by four O_w and two O; Fe2 marked by orange is coordinated by four O_w and

two O. Table I shows the summary of the calculated and experimental key structural results of $\text{Fe}_3(\text{PO}_4)_2 \cdot 8\text{H}_2\text{O}$. The

Table I. Calculated PBE + U (6 eV) Structural Properties of 2D and Bulk $\text{Fe}_3(\text{PO}_4)_2 \cdot 8\text{H}_2\text{O}$ ^a

layer number	a (Å)	b (Å)	c (Å)	β°	$d_{\text{O-O}}$ (Å)
1	10.021		4.625	101.88	
2	9.952		4.633	101.94	2.856
3	9.928		4.632	101.94	2.865
4	9.917		4.632	101.95	2.869
5	9.910		4.632	101.94	2.870
6	9.906		4.633	101.94	2.871
bulk	9.926	13.050	4.616	101.49	2.843
expt ²⁴ for bulk	10.021	13.441	4.721	102.84	2.934

^aLattice parameters a , b , and c are in angstroms and the β angle is in degrees. The equilibrium distance $d_{\text{O-O}}$ is the averaged interlayer O–O distance.

calculated lattice parameters of bulk $\text{Fe}_3(\text{PO}_4)_2 \cdot 8\text{H}_2\text{O}$ displayed in Table I are 2% smaller than the experimental data²⁴ and consistent with the previous reported DFT value.²⁵ The lattice parameters of 2D $\text{Fe}_3(\text{PO}_4)_2 \cdot 8\text{H}_2\text{O}$ are very close to the bulk $\text{Fe}_3(\text{PO}_4)_2 \cdot 8\text{H}_2\text{O}$. The equilibrium distance $d_{\text{O-O}}$ is defined as the averaged interlayer $\text{O}_w\text{-O}_w$ marked by the black ellipse distances. It reflects the strength of the interlayer hydrogen bond and varies from 2.843 to 2.871 Å, decreasing in the order of $6\text{L} > 5\text{L} > 4\text{L} > 3\text{L} > 2\text{L} > \text{bulk}$, and the $d_{\text{O-O}}$ of 4L, 5L, and 6L are almost the same. So the strength of hydrogen bond of bulk $\text{Fe}_3(\text{PO}_4)_2 \cdot 8\text{H}_2\text{O}$ is stronger than all 2D $\text{Fe}_3(\text{PO}_4)_2 \cdot 8\text{H}_2\text{O}$.

B. Electronic Structures of 2D $\text{Fe}_3(\text{PO}_4)_2 \cdot 8\text{H}_2\text{O}$ - (010)-(1 \times 1). The band structures of 2D and bulk $\text{Fe}_3(\text{PO}_4)_2 \cdot 8\text{H}_2\text{O}$ are shown in Figure 2. The bulk $\text{Fe}_3(\text{PO}_4)_2 \cdot 8\text{H}_2\text{O}$ (Figure 2g) has a direct band gap of 4.64 eV. Noticeably, the electronic structures of 2D $\text{Fe}_3(\text{PO}_4)_2 \cdot 8\text{H}_2\text{O}$ show two interesting properties. First, generally speaking, the band gap of 2D materials will increase

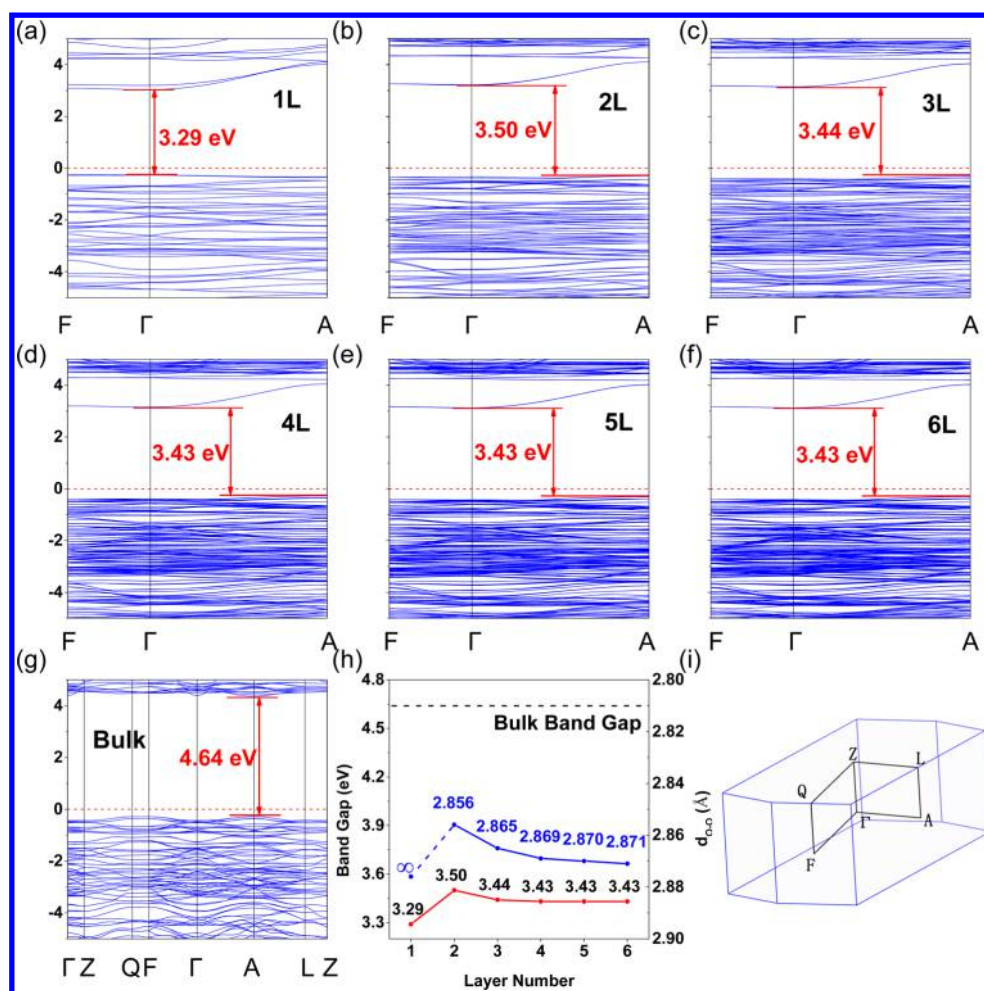


Figure 2. Calculated band structures of (a) monolayer (1L), (b) bilayer (2L), (c) trilayer (3L), (d) quadrilayer (4L), (e) pentilayer (5L), (f) hexilayer (6L), and (g) bulk $\text{Fe}_3(\text{PO}_4)_2 \cdot 8\text{H}_2\text{O}$. The Fermi level shown as the red dashed line is at zero energy. The red arrows indicate the band gap. (h) Band gap energy (red line) and $d_{\text{O-O}}$ (blue line) of 2D $\text{Fe}_3(\text{PO}_4)_2 \cdot 8\text{H}_2\text{O}$ for number of layers $N = 1-6$. As a reference, the band gap energy of bulk $\text{Fe}_3(\text{PO}_4)_2 \cdot 8\text{H}_2\text{O}$ is shown as dashed line. (i) Brillouin zone of bulk $\text{Fe}_3(\text{PO}_4)_2 \cdot 8\text{H}_2\text{O}$.

with decreasing thickness due to quantum confinement. However, the band gap of 2D $\text{Fe}_3(\text{PO}_4)_2 \cdot 8\text{H}_2\text{O}$ is evidently smaller than the bulk $\text{Fe}_3(\text{PO}_4)_2 \cdot 8\text{H}_2\text{O}$, which is opposite to the normal quantum confinement effect. Second, the band gap of monolayer 2D $\text{Fe}_3(\text{PO}_4)_2 \cdot 8\text{H}_2\text{O}$ is much smaller than other 2D layers and bulk $\text{Fe}_3(\text{PO}_4)_2 \cdot 8\text{H}_2\text{O}$, and there is no trend for the band gaps of 2D $\text{Fe}_3(\text{PO}_4)_2 \cdot 8\text{H}_2\text{O}$ to approach the bulk value with the increasing thickness. The band gaps of 4L, 5L, and 6L $\text{Fe}_3(\text{PO}_4)_2 \cdot 8\text{H}_2\text{O}$ are almost the same (3.43 eV).

From Figure 2, we can see the conduction band minimum (CBM) of 2D $\text{Fe}_3(\text{PO}_4)_2 \cdot 8\text{H}_2\text{O}$ along F-point to Γ -point is obviously lower than the bulk (~ 1.2 eV) and shifts to higher energies with the increasing layers, while the valence band maximum (VBM) changes a little (~ 0.02 eV for monolayer and ~ 0.1 eV for others). So the change of conduction band contributes the most to the difference of band structures between the 2D and bulk $\text{Fe}_3(\text{PO}_4)_2 \cdot 8\text{H}_2\text{O}$ and the band gap variations of 2D and bulk $\text{Fe}_3(\text{PO}_4)_2 \cdot 8\text{H}_2\text{O}$. To deeply understand the abnormal phenomenon of the band gap, we further calculate the total and partial density of states (PDOS) on Fe1, Fe2, O, H, and P atoms for 2D and bulk $\text{Fe}_3(\text{PO}_4)_2 \cdot 8\text{H}_2\text{O}$, as shown in Figure 3a. It is found that the shapes of PDOS of 2D and bulk $\text{Fe}_3(\text{PO}_4)_2 \cdot 8\text{H}_2\text{O}$ are roughly equal, and the PDOS of 2D $\text{Fe}_3(\text{PO}_4)_2 \cdot 8\text{H}_2\text{O}$ becomes closer to that of bulk with

increasing layers. The medium valence band (within the energy range of -2 to -10 eV) has three parts, composed of O and H, O and P, and O and Fe, respectively. The VBM (within the energy range of -1 to 0 eV) is composed of Fe, O, and a few H and P. Compared with the PDOS of bulk $\text{Fe}_3(\text{PO}_4)_2 \cdot 8\text{H}_2\text{O}$, in 2D $\text{Fe}_3(\text{PO}_4)_2 \cdot 8\text{H}_2\text{O}$, a small portion of Fe, H, and O states in CBM distributes in the original band gap of the bulk, which results in the change of band gap. As Figure 3b shows, these states mostly come from the edge atoms (Figure 3c). From the PDOS (Figure 3b) of 2D $\text{Fe}_3(\text{PO}_4)_2 \cdot 8\text{H}_2\text{O}$ near Fermi level, we find that the height of edge states on the order of 1.2 to 1.4 states/eV, roughly equal to the sum of the states of Fe, H, and O in monolayer to 6L and invariant with the increasing layers.

Here we adopt a simple model to estimate the effect of quantum confinement in thin film 2D materials qualitatively³⁷⁻³⁹

$$\Delta E_B \approx \frac{\hbar^2}{m^* L^2}$$

where ΔE_B is the energy shift of a bulk state due to the quantum confinement and \hbar and L stand for the reduced Planck constant and the film thickness, respectively. The effective mass of charge carrier m^* is defined as

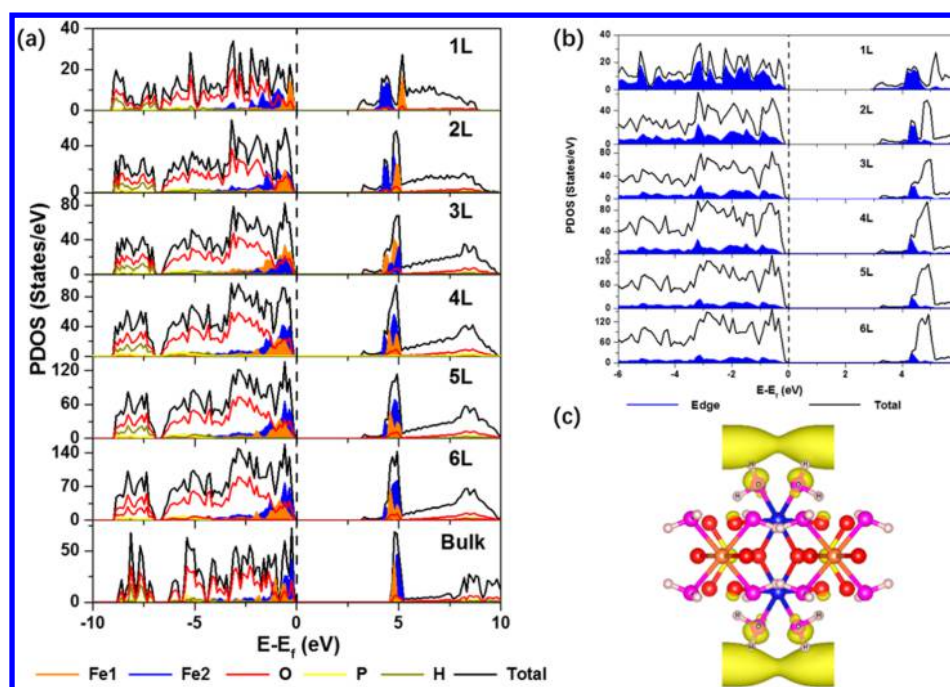


Figure 3. (a) Calculated partial density of states (PDOS) (DOS on specified atoms) and (b) total (black) and edge (blue) DOS of monolayer (1L), bilayer (2L), trilayer (3L), quadrilayer (4L), pentalayer (5L), hexalayer (6L), and bulk Fe₃(PO₄)₂·8H₂O. The Fermi level shown as the black dashed line is at zero energy. (c) Electron density of states of the conduction band minimum (CBM) for the 1L Fe₃(PO₄)₂·8H₂O.

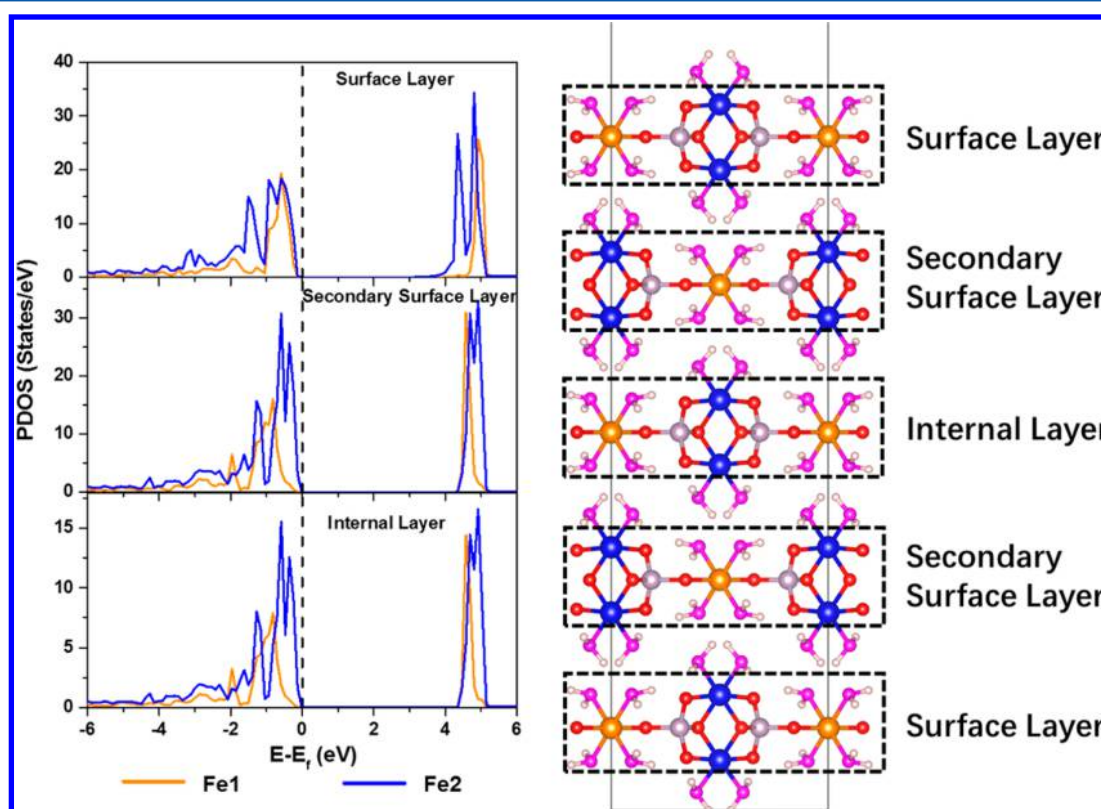


Figure 4. Calculated PDOS of Fe1 and Fe2 of 5L Fe₃(PO₄)₂·8H₂O in surface layer, secondary surface layer, and internal layer.

$$\frac{1}{m^*} = \frac{1}{\hbar^2} \frac{d^2 \varepsilon}{dk^2}$$

where ε is the energy and k is the wave vector. From Figure 2, the effective masses of charge carrier for monolayer Fe₃(PO₄)₂·8H₂O are calculated to be $m_e^* \approx 0.2 m_e$ in CBM and $m_h^* \approx 4.7 m_e$

in VBM, respectively. Compared with other layered 2D materials such as monolayer MoS₂ (0.35 and 0.45 m_e for electron and hole, respectively),⁴⁰ black-phosphorus (0.15 and 0.30 m_e for electron and hole, respectively),⁴¹ and SnS (0.238 and 0.223 m_e for electron and hole, respectively),⁴² the effective mass of hole is much larger for monolayer Fe₃(PO₄)₂·8H₂O, while their

effective masses of electron are comparable. However, the L of monolayer $\text{Fe}_3(\text{PO}_4)_2 \cdot 8\text{H}_2\text{O}$ is $\sim 7.5 \text{ \AA}$, which is much larger than them (3.10 \AA for MoS_2 , 2.26 \AA for black-phosphorus, and 2.86 \AA for SnS). This would lead to a much weaker quantum confinement ($\Delta E_{\text{B}} \approx 1/L^2$). So the edge state is the dominating effect to the reduced band gaps in few-layer 2D $\text{Fe}_3(\text{PO}_4)_2 \cdot 8\text{H}_2\text{O}$.

From the band structures (Figure 2), we also notice that the CBM splits at Γ - Γ line by $\sim 0.17 \text{ eV}$ at Γ -point for monolayer, while the splitting is only $\sim 0.02 \text{ eV}$ at Γ -point for bilayer and 0.002 eV for 3L to 6L, and no splitting at Γ -point is found in bulk. This is the main reason accounting for the much smaller band gap of monolayer than that of other layers. Furthermore, from the PDOS, we can see the position of peaks of Fe2 is lower than that of Fe1 in monolayer at both VBM and CBM and is shifted to higher energies and overlap the peaks of Fe1 as layers increase, leading to enlarged band gaps. Thus it can be concluded that the splitting of CBM mainly comes from the degenerated energy levels of Fe1 and Fe2 with different coordinations. It is because that Fe–O bond (2.02 \AA) is stronger than Fe– O_{w} bond (2.06 \AA) in the surface layer, while they become nearly the same in internal layers and bulk $\text{Fe}_3(\text{PO}_4)_2 \cdot 8\text{H}_2\text{O}$. To testify this assumption, we give the PDOS of Fe1 and Fe2 of 5L $\text{Fe}_3(\text{PO}_4)_2 \cdot 8\text{H}_2\text{O}$ in surface layer, secondary surface layer, and internal layer, respectively (Figure 4). The positions of peaks of Fe1 and Fe2 in secondary surface layer and internal layer are very similar to their position in bulk, corresponding with the same strength of Fe–O bond (2.03 \AA) and Fe– O_{w} bond (2.03 \AA), and the position of peak of Fe2 is lower than that of Fe1 in surface layer at CBM. So the phenomenon of PDOS of Fe1 and Fe2, the one tending to overlap in the multilayer, can be attributed to the increasing Fe1 and Fe2 number in the internal layers.

Because the space group of monolayer is the same as other odd layers and the obvious split for CBM is only observed in monolayer, it is reasonable to infer that the layered hydrogen-bond interaction accounts for the reduced splitting of CBM in 2D ($>1\text{L}$) and bulk $\text{Fe}_3(\text{PO}_4)_2 \cdot 8\text{H}_2\text{O}$. To testify this inference, we fix the $d_{\text{O-O}} = 3.550$ and 4.550 \AA and calculate the band structure of bilayer $\text{Fe}_3(\text{PO}_4)_2 \cdot 8\text{H}_2\text{O}$. As shown in Figure S1, the band gap with different $d_{\text{O-O}}$ is 3.50 , 3.48 , and 3.30 eV , respectively, and the splitting of CBM is 0.017 , 0.025 , and 0.104 eV , respectively. For bilayer $\text{Fe}_3(\text{PO}_4)_2 \cdot 8\text{H}_2\text{O}$, it is obvious that the weaker hydrogen bond leads to the smaller band gap and larger splitting of CBM. The reduced splitting of CBM can be attributed to the layered hydrogen-bond interaction inducing a built-in electric field, which lifts the energy levels of the Fe2 at the edge and tunes the edge states for 2D $\text{Fe}_3(\text{PO}_4)_2 \cdot 8\text{H}_2\text{O}$. Thus it is also reasonable to assume that the abnormal phenomenon of the band gap of 2D $\text{Fe}_3(\text{PO}_4)_2 \cdot 8\text{H}_2\text{O}$ could be related to the strength of interlayer hydrogen bonds. Figure 2h shows the trend of band gaps and interlayer $d_{\text{O-O}}$ of 2D $\text{Fe}_3(\text{PO}_4)_2 \cdot 8\text{H}_2\text{O}$. It can be found that the band gap varies from 3.29 to 4.64 eV , decreasing in the order of bulk $>2\text{L} > 3\text{L} > 4\text{L} \approx 5\text{L} \approx 6\text{L} > 1\text{L}$. Because there are no interlayer hydrogen bonds for monolayer $\text{Fe}_3(\text{PO}_4)_2 \cdot 8\text{H}_2\text{O}$, for comparison with other 2D few-layers, here we assume the interlayer $d_{\text{O-O}}$ is ∞ for monolayer $\text{Fe}_3(\text{PO}_4)_2 \cdot 8\text{H}_2\text{O}$. Then, indeed, the order of interlayer $d_{\text{O-O}}$ ($1\text{L} > 6\text{L} \approx 5\text{L} \approx 4\text{L} > 3\text{L} > 2\text{L}$) is just the reverse to the order of band gaps for 2D $\text{Fe}_3(\text{PO}_4)_2 \cdot 8\text{H}_2\text{O}$, and the stronger hydrogen bond corresponds to larger band gap for 2D $\text{Fe}_3(\text{PO}_4)_2 \cdot 8\text{H}_2\text{O}$. For the edge layer, because of the absence of the force from outside layers, the strength of hydrogen bond with the inside layer becomes stronger, making the $d_{\text{O-O}}$ of bulk larger than 2D

$\text{Fe}_3(\text{PO}_4)_2 \cdot 8\text{H}_2\text{O}$. For the same reason, the interlayer $d_{\text{O-O}}$ of bilayer $\text{Fe}_3(\text{PO}_4)_2 \cdot 8\text{H}_2\text{O}$, which does not have any outside layers, is smaller than other 2D few-layers. With the increasing layers, the force from outside layers becomes changeless, so the interlayer $d_{\text{O-O}}$ of 4L, 5L, and 6L $\text{Fe}_3(\text{PO}_4)_2 \cdot 8\text{H}_2\text{O}$ only have a tiny difference. As a result, the band gaps of 4L, 5L, and 6L $\text{Fe}_3(\text{PO}_4)_2 \cdot 8\text{H}_2\text{O}$ are almost the same.

IV. CONCLUSIONS

This work presented a theoretical study of the structural and electronic properties of the new hydrogen-bonded 2D vivianite $\text{Fe}_3(\text{PO}_4)_2 \cdot 8\text{H}_2\text{O}$ for the first time. 2D $\text{Fe}_3(\text{PO}_4)_2 \cdot 8\text{H}_2\text{O}$ has a tunable band gap from ~ 3.29 to 3.50 eV , which is smaller than the bulk (4.64 eV). The contradiction with the normal quantum confinement effect is due to the tiny quantum confinement and the prominent edge states in 2D $\text{Fe}_3(\text{PO}_4)_2 \cdot 8\text{H}_2\text{O}$. The edge states composed of the surface atoms distribute in the original band gap of bulk $\text{Fe}_3(\text{PO}_4)_2 \cdot 8\text{H}_2\text{O}$, leading to the splitting at the CBM and the reduced band gap for 2D $\text{Fe}_3(\text{PO}_4)_2 \cdot 8\text{H}_2\text{O}$ with decreasing layers. The strength of interlayer hydrogen bond can tune the band gaps of 2D $\text{Fe}_3(\text{PO}_4)_2 \cdot 8\text{H}_2\text{O}$ by tuning the edge states.

■ ASSOCIATED CONTENT

Supporting Information

The Supporting Information is available free of charge on the ACS Publications website at DOI: 10.1021/acs.jpcc.6b07481.

Table S1. Calculated different magnetism of 1L, 2L and 3L $\text{Fe}_3(\text{PO}_4)_2 \cdot 8\text{H}_2\text{O}$. Figure S1. Calculated band structures of 2L $\text{Fe}_3(\text{PO}_4)_2 \cdot 8\text{H}_2\text{O}$ with $d_{\text{O-O}} = 2.856$, 3.550 , and 4.550 \AA . (PDF)

■ AUTHOR INFORMATION

Corresponding Authors

*J.Z.: E-mail: zhengjx@pkusz.edu.cn.

*F.P.: E-mail: panfeng@pkusz.edu.cn.

ORCID

Sibai Li: 0000-0002-4301-132X

Notes

The authors declare no competing financial interest.

■ ACKNOWLEDGMENTS

The work was financially supported by National Materials Genome Project (2016YFB0700600), Guangdong Innovation Team Project (No. 2013N080), and Shenzhen Science and Technology Research Grant (Nos. ZDSY20130331145131323, JCYJ20140903101633318, JCYJ20140903101617271).

■ REFERENCES

- (1) Novoselov, K. S.; Geim, A. K.; Morozov, S. V.; Jiang, D.; Zhang, Y.; Dubonos, S. V.; Grigorieva, I. V.; Firsov, A. A. Electric Field Effect in Atomically Thin Carbon Films. *Science* **2004**, *306*, 666–669.
- (2) Larentis, S.; Fallahzad, B.; Tutuc, E. Field-Effect Transistors and Intrinsic Mobility in Ultra-Thin MoSe_2 Layers. *Appl. Phys. Lett.* **2012**, *101*, 223104.
- (3) Radisavljevic, B.; Radenovic, A.; Brivio, J.; Giacometti, V.; Kis, A. Single-Layer MoS_2 Transistors. *Nat. Nanotechnol.* **2011**, *6*, 147–150.
- (4) Pan, Y.; Li, S.; Ye, M.; Quhe, R.; Song, Z.; Wang, Y.; Zheng, J.; Pan, F.; Guo, W.; Yang, J.; et al. Interfacial Properties of Monolayer MoSe_2 –Metal Contacts. *J. Phys. Chem. C* **2016**, *120*, 13063–13070.
- (5) Sharma, D.; Amani, M.; Motayed, A.; Shah, P. B.; Birdwell, A. G.; Najmaei, S.; Ajayan, P. M.; Lou, J.; Dubey, M.; Li, Q.; et al. Electrical

Transport and Low-Frequency Noise in Chemical Vapor Deposited Single-Layer MoS₂ Devices. *Nanotechnology* **2014**, *25*, 155702.

(6) Tian, L.-L.; Li, S.-B.; Zhang, M.-J.; Li, S.-K.; Lin, L.-P.; Zheng, J.-X.; Zhuang, Q.-C.; Amine, K.; Pan, F. Cascading Boost Effect on the Capacity of Nitrogen-Doped Graphene Sheets for Li- and Na-Ion Batteries. *ACS Appl. Mater. Interfaces* **2016**, *8*, 26722–26729.

(7) Peng, L.; Peng, X.; Liu, B.; Wu, C.; Xie, Y.; Yu, G. Ultrathin Two-Dimensional MnO₂/Graphene Hybrid Nanostructures for High-Performance, Flexible Planar Supercapacitors. *Nano Lett.* **2013**, *13*, 2151–2157.

(8) Zeng, H.; Dai, J.; Yao, W.; Xiao, D.; Cui, X. Valley Polarization in MoS₂ Monolayers by Optical Pumping. *Nat. Nanotechnol.* **2012**, *7*, 490–493.

(9) Wang, Q. H.; Kalantar-Zadeh, K.; Kis, A.; Coleman, J. N.; Strano, M. S. Electronics and Optoelectronics of Two-Dimensional Transition Metal Dichalcogenides. *Nat. Nanotechnol.* **2012**, *7*, 699–712.

(10) Chhowalla, M.; Shin, H. S.; Eda, G.; Li, L.-J.; Loh, K. P.; Zhang, H. The Chemistry of Two-Dimensional Layered Transition Metal Dichalcogenide Nanosheets. *Nat. Chem.* **2013**, *5*, 263–275.

(11) Schaak, R. E.; Mallouk, T. E. Prying Apart Ruddlesden–Popper Phases: Exfoliation into Sheets and Nanotubes for Assembly of Perovskite Thin Films. *Chem. Mater.* **2000**, *12*, 3427–3434.

(12) Kim, T. W.; Oh, E.-J.; Jee, A.-Y.; Lim, S. T.; Park, D. H.; Lee, M.; Hyun, S.-H.; Choy, J.-H.; Hwang, S.-J. Soft-Chemical Exfoliation Route to Layered Cobalt Oxide Monolayers and Its Application for Film Deposition and Nanoparticle Synthesis. *Chem. - Eur. J.* **2009**, *15*, 10752–10761.

(13) Hu, L.; Ma, R.; Ozawa, T. C.; Sasaki, T. Exfoliation of Layered Europium Hydroxide into Unilamellar Nanosheets. *Chem. - Asian J.* **2010**, *5*, 248–251.

(14) Splendiani, A.; Sun, L.; Zhang, Y.; Li, T.; Kim, J.; Chim, C. Y.; Galli, G.; Wang, F. Emerging Photoluminescence in Monolayer MoS₂. *Nano Lett.* **2010**, *10*, 1271–1275.

(15) Liu, T.; Feng, Y.; Duan, Y.; Cui, S.; Lin, L.; Hu, J.; Guo, H.; Zhuo, Z.; Zheng, J.; Lin, Y.; et al. Formation of Mono/Bi-Layer Iron Phosphate and Nucleation of LiFePO₄ Nano-Crystals from Amorphous 2D Sheets in Charge/Discharge Process for Cathode in High-Performance Li-Ion Batteries. *Nano Energy* **2015**, *18*, 187–195.

(16) Liu, T.; Duan, Y.; Zhang, G.; Li, M.; Feng, Y.; Hu, J.; Zheng, J.; Chen, J.; Pan, F. 2D Amorphous Iron Phosphate Nanosheets with High Rate Capability and Ultra-Long Cycle Life for Sodium Ion Batteries. *J. Mater. Chem. A* **2016**, *4*, 4479–4484.

(17) Townsend, M. G.; Faye, G. H. Polarised Electronic Absorption Spectrum of Vivianite. *Phys. Status Solidi B* **1970**, *38*, K57–K60.

(18) Taran, M. N.; Platonov, A. N. Optical Absorption Spectra of Iron Ions in Vivianite. *Phys. Chem. Miner.* **1988**, *16*, 304–310.

(19) Kleinberg, R. Magnetic Structure of Vivianite Fe₃(PO₄)₂·8H₂O. *J. Chem. Phys.* **1969**, *51*, 2279.

(20) Gonser, U.; Grant, R. W. Determination of Spin Directions and Electric Field Gradient Axes in Vivianite by Polarized Recoil-Free γ -Rays. *Phys. Status Solidi B* **1967**, *21*, 331–342.

(21) Van der Lugt, W.; Poullis, N. J. The Splitting of the Nuclear Magnetic Resonance Lines in Vivianite. *Physica* **1961**, *27*, 733–750.

(22) Meijer, H. C.; Van den Handel, J.; Frikkee, E. Magnetic Behaviour of Vivianite, Fe₃(PO₄)₂·8H₂O. *Physica* **1967**, *34*, 475–483.

(23) Piriou, B.; Poullien, J. F. Raman Study of Vivianite. *J. Raman Spectrosc.* **1984**, *15*, 343–346.

(24) Bartl, H. Water of Crystallization and Its Hydrogen-Bonded Crosslinking in Vivianite Fe₃(PO₄)₂·8H₂O; a Neutron Diffraction Investigation. *Fresenius' Z. Anal. Chem.* **1989**, *333*, 401–403.

(25) Pinto, H. P.; Michalkova, A.; Leszczynski, J. First-Principles Studies of Paramagnetic Vivianite Fe₃(PO₄)₂·8H₂O Surfaces. *J. Phys. Chem. C* **2014**, *1183*, 6110–6121.

(26) Grodzicki, M.; Amthauer, G. Electronic and Magnetic Structure of Vivianite: Cluster Molecular Orbital Calculations. *Phys. Chem. Miner.* **2000**, *27*, 694–702.

(27) Frederichs, T.; von Dobeneck, T.; Bleil, U.; Dekkers, M. J. Towards the Identification of Siderite, Rhodochrosite, and Vivianite in

Sediments by Their Low-Temperature Magnetic Properties. *Phys. Chem. Earth, Parts A/B/C* **2003**, *28*, 669–679.

(28) Frost, R. L.; Weier, M. Raman Spectroscopic Study of Vivianites of Different Origins. *Neues Jahrb. Mineral, Monatsh.* **2004**, *2004*, 445–463.

(29) Blöchl, P. E. Projector Augmented-Wave Method. *Phys. Rev. B: Condens. Matter Mater. Phys.* **1994**, *50*, 17953–17979.

(30) Kresse, G.; Joubert, D. From Ultrasoft Pseudopotentials to the Projector Augmented-Wave Method. *Phys. Rev. B: Condens. Matter Mater. Phys.* **1999**, *59*, 1758–1775.

(31) Kresse, G.; Furthmüller, J. Efficient Iterative Schemes for Ab Initio Total-Energy Calculations Using a Plane-Wave Basis Set. *Phys. Rev. B: Condens. Matter Mater. Phys.* **1996**, *54*, 11169–11186.

(32) Kresse, G.; Furthmüller, J. Efficiency of Ab-Initio Total Energy Calculations for Metals and Semiconductors Using a Plane-Wave Basis Set. *Comput. Mater. Sci.* **1996**, *6*, 15–50.

(33) Perdew, J. P.; Burke, K.; Ernzerhof, M. Generalized Gradient Approximation Made Simple. *Phys. Rev. Lett.* **1996**, *77*, 3865–3868.

(34) Liechtenstein, A. I.; Anisimov, V. I.; Zaanen, J. Density-Functional Theory and Strong Interactions: Orbital Ordering in Mott-Hubbard Insulators. *Phys. Rev. B: Condens. Matter Mater. Phys.* **1995**, *52*, R5467–R5470.

(35) Monkhorst, H. J.; Pack, J. D. Special Points for Brillouin-Zone Integrations. *Phys. Rev. B* **1976**, *13*, 5188–5192.

(36) Moriya, T. Theory of Itinerant Electron Magnetism. *J. Magn. Mater.* **1991**, *100*, 261–271.

(37) Martelli, F.; Capizzi, M.; Frova, A.; Polimeni, A.; Sarto, F.; Bruni, M. R.; Simeone, M. G. Exciton Confinement in GaAs Quantum Barriers. *Phys. Rev. B: Condens. Matter Mater. Phys.* **1993**, *48*, 1643–1646.

(38) Gulia, V.; Vedeshwar, A. G.; Mehra, N. C. Quantum Dot-like Behavior of Ultrathin PbI₂ Films. *Acta Mater.* **2006**, *54*, 3899–3905.

(39) Arivazhagan, V.; Parvathi, M. M.; Rajesh, S.; Sæterli, R.; Holmestad, R. Quantum Confinement in Two Dimensional Layers of PbSe/ZnSe Multiple Quantum Well Structures. *Appl. Phys. Lett.* **2013**, *102*, 242110.

(40) Cheiwchanamngij, T.; Lambrecht, W. R. L. Quasiparticle Band Structure Calculation of Monolayer, Bilayer, and Bulk MoS₂. *Phys. Rev. B: Condens. Matter Mater. Phys.* **2012**, *85*, 1–4.

(41) Qiao, J.; Kong, X.; Hu, Z.-X.; Yang, F.; Ji, W. High-Mobility Transport Anisotropy and Linear Dichroism in Few-Layer Black Phosphorus. *Nat. Commun.* **2014**, *5*, 4475.

(42) Xin, C.; Zheng, J.; Su, Y.; Li, S.; Zhang, B.; Feng, Y.; Pan, F. Few-Layer Tin Sulfide: A New Black-Phosphorus Analogue 2D Material with a Sizeable Band Gap, Odd–Even Quantum Confinement Effect, and High Carrier Mobility. *J. Phys. Chem. C* **2016**, *120*, 22663–22669.